ACS APPLIED NANO MATERIALS

www.acsanm.org Article

Large Superparamagnetic FeCo Nanocubes for Magnetic Theranostics

Jinming Liu,[†] Kai Wu,[†] Shihai He, Jianmin Bai, Yun-Hao Xu, and Jian-Ping Wang*

Cite This: *ACS Appl. Nano Mater.* 2021, 4, 9382−9390 Read Online

ACCESS | Metrics & More | Article Recommendations | Supporting Information

ABSTRACT: In the past few decades, superparamagnetic nanoparticles (SPMNPs) have attracted increasing attention in a wide range of magnetic theranostics including magnetic biosensors, drug delivery, magnetic separation, magnetic imaging, hyperthermia therapy, and so on. Superparamagnetic iron oxide nanoparticles are currently widely used for these purposes despite their low saturation magnetizations (below 80 emu/g). In pursuit of higher magnetic signals (spatial resolutions) for magnetic imaging, higher sensitivity (limit of detection) for biosensing, higher efficiency, and lower dosage in drug delivery and hyperthermia therapy, magnetic compounds and alloys that generally have higher saturation magnetizations are of interest. FeCo SPMNPs are considered promising candidates for biomedical applications due to their good corrosion resistance, stability, and high saturation magnetizations (over 220 emu/g). However, the critical size for FeCo nanoparticles to be superparamagnetic is limited by a theoretical value of ∼15 nm, making it difficult to further increase the magnetic moment per SPMNP. Herein, we report a method to synthesize large single-crystalline FeCo nanoparticle complexes (NPCs) with an overall size of ∼100 nm while retaining the superparamagnetic properties. These large FeCo NPCs are synthesized by self-assembling 3 nm FeCo nanoparticle units through a DC sputtering-based gas-phase condensation (GPC) method. By controlling the sputtering parameters like sputtering current density, sputtering pressure, and carrying gas velocity in the GPC system, the nucleation and growth of FeCo nanoparticles can be tuned, and different sizes of nanoparticles can be obtained. The large FeCo NPCs are formed from the second crystallization of small FeCo nanoparticle units with well-aligned crystalline axes, which show both high saturation magnetization and superparamagnetic properties suitable for biomedical applications. It is expected that with the superparamagnetic behavior and higher magnetic moment per FeCo NPC, they can potentially bring higher sensitivities to magnetic biosensors that rely on the magnetic labels, higher efficiency in hyperthermia therapy, and lower dose requirements for magnetic imaging and separation.

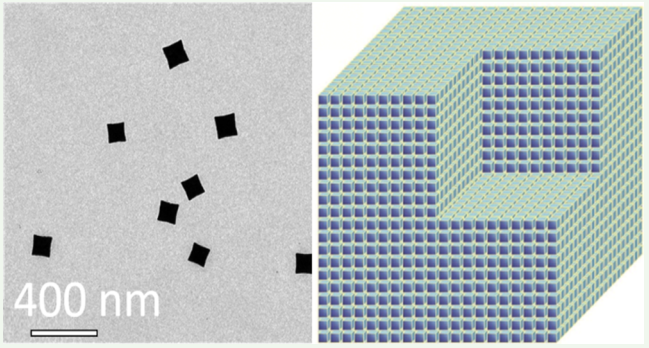

KEYWORDS: *gas-phase condensation, superparamagnetic, high moment, nanoparticle complexes, biomedical applications*

1. INTRODUCTION

Nowadays, superparamagnetic nanoparticles (SPMNPs) play an important role in a variety of magnetic theranostics such as magnetic biosensors,[1−6] hyperthermia therapy,[7−11] magnetic resonance imaging,[12−15] and drug delivery.[16−19] The performances of these applications largely depend on the magnetic properties of SPMNPs regarding their physicochemical stability, cytotoxicity, size, and magnetic moment per particle.[1,20] Currently, superparamagnetic iron oxide nanoparticles (SPIONs) are prevalently used for these applications due to their ease of synthesis, inexpensiveness, controllable size, biocompatibility, and cytotoxicity. However, the saturation magnetizations of SPIONs reported are below 80 emu/g, limiting the magnetic moment per particle.[21,22] Alternatively magnetic compounds and alloys that show higher saturation magnetizations are being explored to provide alternative choices besides iron oxide in views of higher magnetic signals. FeCo is considered one of the candidate materials.[23] It has the highest saturation magnetization (of all SPMNPs) based on Slater−Pauling curves.[24−26] In addition, by coating FeCo MNPs with biocompatible layers, their cytotoxicity issues can be solved.[1,27−31] However, magnetic moment per particle is not only dependent on the saturation magnetization of a material but also on the magnetic core sizes of nanoparticles. For MNPs to maintain superparamagnetic properties at room temperature, their magnetic core sizes should be smaller than a critical size, which varies for different magnetic materials.[32,33]

Received: July 9, 2021
Accepted: August 23, 2021
Published: September 1, 2021

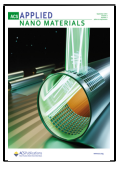

https://doi.org/10.1021/acsanm.1c01870
ACS Appl. Nano Mater. 2021, 4, 9382−9390

For example, the critical size for iron oxide nanoparticles to be superparamagnetic is around 25 nm, while it is 15 nm for FeCo nanoparticles.[34] Thus, the requirement of superparamagnetic property limits the largest size of FeCo nanoparticles and the largest possible magnetic moment per particle that we can achieve for biomedical applications.

Self-assembling smaller SPMNPs, namely, smaller nanoparticle units, into larger magnetic nanoparticle complexes (NPCs) is one option to synthesize larger size MNPs while maintaining the superparamagnetic behaviors.[35,36] Chemical methods have been developed either to produce colloidal crystals,[37] or to self-assemble smaller nanoparticles into three-dimensional (3D) arrays with controllable distances between nanoparticle units.[38−40] For example, Hugounenq et al. reported the chemical synthesis of flower-shaped NPCs that constituted of smaller grains of approximately 11 nm.[41] These flower-shaped NPCs show interesting magnetic properties and a great capacity of heating. Besides the chemical methods, self-assembled Mo and Mo−Cu bimetallic nanoparticles using a physical gas-phase condensation (GPC) method have also been reported.[42,43] The superparamagnetic behavior of NPCs might come from the cooperative phenomenon of the interaction of magnetic domains, which was reported by Gazeau et al. on iron oxide multi-core nanoparticles.[44] A magnetic vertex structure can be formed in a NPC with superparamagnetic behavior because of the weak magnetic exchange interactions between the small building blocks of an NPC, which is demonstrated by micromagnetic simulation in this article.

So far, neither the formation mechanism of the self-assembling NPCs nor the functional applications have been reported using a GPC technique. In contrast to conventional nanoparticle synthesis approaches (i.e., colloidal method), this GPC technique can individually control the nucleation and growth stages of nanoparticles in both time and space domains by adjusting the gas pressure, velocity, and sputtering power density.[45−54] On the other hand, it can strictly control the dimensions of spaces related to the glow discharge effect, including the cathode dark space (CDS) and negative glow (NG) region, by adjusting gas pressure, gas flow configuration, and sputtering power density. Thus, the FeCo NPCs can be synthesized by controlling the interaction between these two spaces. Herein, a GPC method was used to synthesize large (∼100 nm), cubic FeCo NPCs that exhibit superparamagnetic behavior at room temperature. The formation mechanisms of the 3D self-assembled FeCo NPCs were proposed which related to the glow discharge effect in the GPC technique.

2. EXPERIMENTAL SECTION

2.1. Synthesis of FeCo NPCs by a GPC Method. A schematic drawing of the GPC system is shown in Figure 1. Fe and Co atoms produced by a dc magnetron sputtering source start to nucleate and grow to form nanoparticles. A plate with an orifice separates the system into two chambers: the sputtering chamber containing a sputtering source to synthesize nanoparticles and the deposition chamber with a substrate to collect these nanoparticles. A pump keeps pumping at the end of the deposition chamber to make a pressure differential between these two chambers, and the synthesized nanoparticles will be carried by the gas flow through the orifice and deposited on a substrate. An $Fe_{60}Co_{40}$ alloy target was used in the DC sputtering-based GPC system as the source material to prepare the FeCo NPCs. The base pressure of the GPC system was $\sim 10^{-7}$ Torr, and ultrapure argon (99.999%) gas was used as the sputtering and carrying gas. A high sputtering pressure of 450 mTorr was applied to enhance the collision rates between sputtered atoms and the argon atoms. The collision transfers the energy of the sputtered atoms to the argon atoms, so that the temperature of the sputtered atoms drops, which allows the nucleation and growth of nanoparticles/NPCs to occur. The details of the GPC system can be found in our previous studies.[55,56]

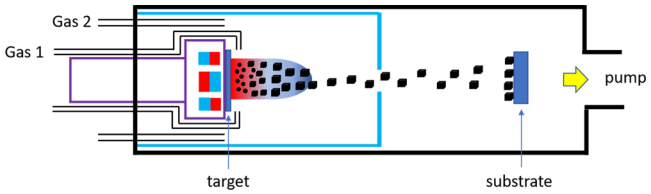

Figure 1. Schematic drawing of the GPC system. Target atoms produced by a dc magnetron sputtering source start the nucleation and growth processes near the target surface. A plate with an orifice separated the system into two chambers: the sputtering chamber containing a sputtering source and a deposition chamber with the substrate to collect the synthesized nanoparticles.

2.2. Phase and Morphology Characterizations of FeCo NPCs and Nanoparticles. The phase information and morphology of FeCo nanoparticles and NPCs were characterized by a transmission electron microscopy (TEM). Briefly, the synthesized FeCo nanoparticles and NPCs were carried by argon gas flow in the GPC system. A TEM grid was placed in the path of nanoparticles and NPCs for collection. Then, the TEM grid was transferred into a transmission electron microscope for the characterizations. During the transfer process, nanoparticles and NPCs were exposed to air, and a very thin native oxidation layer could be observed from the TEM images.

2.3. Magnetic Property Characterizations of FeCo NPCs and Nanoparticles. The magnetic properties of FeCo nanoparticles and NPCs were measured using a superconducting quantum interference device (SQUID) at room temperature. The nanoparticles and NPCs were collected on a small piece of the silicon substrate for the magnetic characterizations. A capping layer was applied to protect the nanoparticles and NPCs from oxidation after taking them out of the high vacuum chambers of the GPC system.

3. RESULTS AND DISCUSSION

3.1. Crystal Structure and Morphology Characterizations of Synthesized FeCo NPCs. Figure 2 shows the TEM images of synthesized FeCo NPCs. From the zoom-out view in Figure 2a, we can see that these FeCo NPCs are cubic with an average size of around 100 nm. Figure 2b shows the zoom-in image of one FeCo NPC, and its diffraction pattern is shown in Figure 2c. The diffraction pattern indicates that these FeCo NPCs are single crystal, which matches well with the body-centered cubic (bcc) FeCo structure with the zone axis of [001]. A dark-field image of the large FeCo NPC is shown in Figure 2d. The black and white contrast in the nanocrystal indicates that each NPC is an assembly of smaller FeCo nanoparticle units. The single-crystal diffraction pattern, as shown in Figure 2c, proves that the crystal axes of these FeCo nanoparticle units are perfectly aligned when forming the large, cubic NPCs.

Furthermore, the FeCo NPC is titled 45° and its diffraction pattern is characterized, as shown in Figure 2e,f. A hexagonal shape is observed due to the titling, and the edge length relationship between top-view and tilted images matches the cubic shape. Importantly, the diffraction pattern of the tilted FeCo NPC confirms the good 3D crystal axis alignment of the FeCo nanoparticles. The TEM results prove that bcc FeCo nanoparticles as building blocks can be self-assembled perfectly to produce large, cubic FeCo NPCs using a GPC method.

https://doi.org/10.1021/acsanm.1c01870
ACS Appl. Nano Mater. 2021, 4, 9382−9390

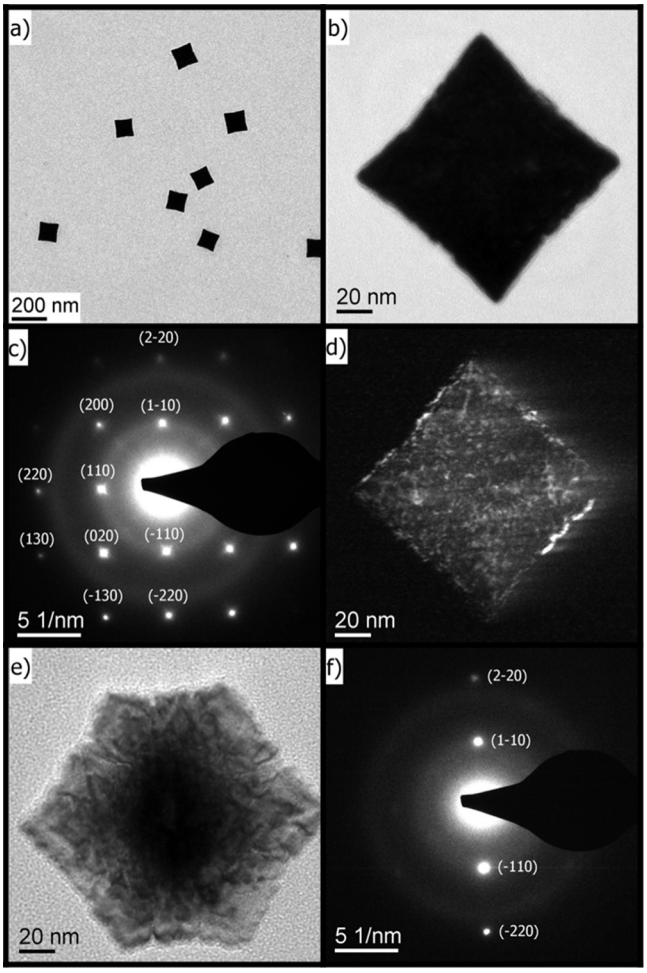

Figure 2. FeCo NPCs synthesized using a GPC method with an average size of ~100 nm. (a) Zoom-out TEM image of the NPCs. One large, cubic FeCo NPC visualized in a bright field (b); its electron diffraction pattern (c); dark field (d). A 45-degree tilted bright-field image of large, cubic FeCo NPC (e) and its electron diffraction pattern (f).

3.2. Comparison between FeCo NPCs, Nanoparticles, and Nanocomposites. Figure 3 gives schematic views of three types of FeCo nanoparticles: a NPC (Figure 3a), a single-crystalline nanoparticle (Figure 3b), and a nanocomposite (Figure 3c). The FeCo NPC, as shown in Figure 3a, is an assembly of identically sized and crystal axes perfectly aligned FeCo nanoparticle units in a 3D array. It is a representation of the large, cubic FeCo NPCs we synthesized in this work. Figure 3b shows a single-crystalline FeCo nanoparticle of identical size and shape to the FeCo NPC counterpart. Figure 3c shows a FeCo nanocomposite consisting of FeCo nanoparticles randomly distributed and oriented (in view of their crystal axes) in a polymer matrix.

Compared with the single-crystalline FeCo nanoparticle, as shown in Figure 3b, the FeCo nanoparticle units from the FeCo NPC, as shown in Figure 3a, lack the solid contact, and therefore, both high surface area to volume ratio and weak inter-particle magnetic exchange interactions can be expected. On the other hand, compared with the FeCo nanocomposite, as shown in Figure 3c, where the FeCo nanoparticles are randomly embedded in polymers, the nanoparticle units, as shown in Figure 3a, are much closer to each other with aligned crystalline axes.[37] Therefore, the FeCo NPC provides a much higher magnetic stray field than that of a FeCo nanocomposite of identical size.

The schematic drawing of the $M-H$ curves of these three different kinds of particles are presented in Figure 3d–f for the FeCo NPC, single-crystalline nanoparticle, and nanocomposite, respectively. Both NPC and the single-crystalline nanoparticle have higher saturation magnetizations due to the high-volume ratio of magnetic cores, as shown in Figure 3d,e. Importantly, the NPC has a lower magnetic coercivity, making it more desirable for biomedical applications. The $M-H$ curve of the nanocomposite, as shown in Figure 3f, indicates that it is superparamagnetic, but its saturation magnetization is much lower than that of the NPC and single-crystalline nanoparticle because of the lower packing density of the small nanoparticle units. Due to the random orientation of the crystal axes of the small nanoparticle units, the nanocomposite has lower stray field intensity compared with the other two, as schematically illustrated in Figure 3g–i. Because of these outlined properties, the FeCo NPC is a promising candidate for biomedical applications.

3.3. Superparamagnetic Properties of 100 nm FeCo NPCs. We first carried out mathematical modeling and experimental measurements on the $M-H$ curves of 3 and 20 nm FeCo single-crystalline nanoparticles, as given in Supporting Information S1. Experimental results show that the 3 nm FeCo nanoparticles are superparamagnetic at room temperature. These nanoparticles are the small building blocks of the large FeCo NPCs (more details are in the following Section 3.5). The 20 nm FeCo single-crystalline nanoparticles, however, show a coercivity of around 40 Oe, indicating that at least some nanoparticles with the size of 20 nm are ferromagnetic, which is consistent with the distribution of the magnetic anisotropy of FeCo related to the different compositions.

Interestingly, the 100 nm large, cubic FeCo NPCs show a very similar trend of hysteresis loop to that of 3 nm FeCo nanoparticles, as shown in Figure 4a. A 3 nm FeCo nanoparticle, containing around 1000 atoms, is very close to the FeCo nanoparticle units that form NPCs in this work. The hysteresis loop of large FeCo NPCs has a small coercivity of around 100 Oe, as shown in Figure 4b, the zoom-in view of Figure 4a. The saturation magnetization is around 1650 emu/cm^3 (~200 emu/g). The ratio of remanent magnetization to saturation magnetization, M_r/M_s, is only 6%, indicating the weak exchange interactions between the FeCo nanoparticles.

3.4. Magnetization Patterns of Large, Cubic FeCo NPCs Revealed by Micromagnetic Simulations. Micromagnetic simulations are carried out on the large, cubic FeCo NPCs using the Object Oriented Micromagnetic Framework to explain their superparamagnetic behavior. Due to the lack of solid contact between these 3 nm nanoparticle units, the magnetic exchange interactions between these units are reduced. A magnetic vortex can be induced in FeCo NPCs, reducing the coercivity and M_r/M_s ratio to achieve the superparamagnetic behavior. As a demonstration, we carried out the micromagnetic simulation at 0 K on one 3 nm FeCo nanoparticle and one 40 nm FeCo NPC with a 10 × 10 × 10 array of 3 nm FeCo nanoparticle units. The gap between the 3 nm FeCo nanoparticles was set at 1 nm to simulate the reduced exchange interactions between these nanoparticle units. The simulated $M-H$ curves and magnetization patterns under different fields are shown in Figure 5. As shown in Figure 5a, the 3 nm FeCo nanoparticle shows ferromagnetic

https://doi.org/10.1021/acsanm.1c01870
ACS Appl. Nano Mater. 2021, 4, 9382–9390

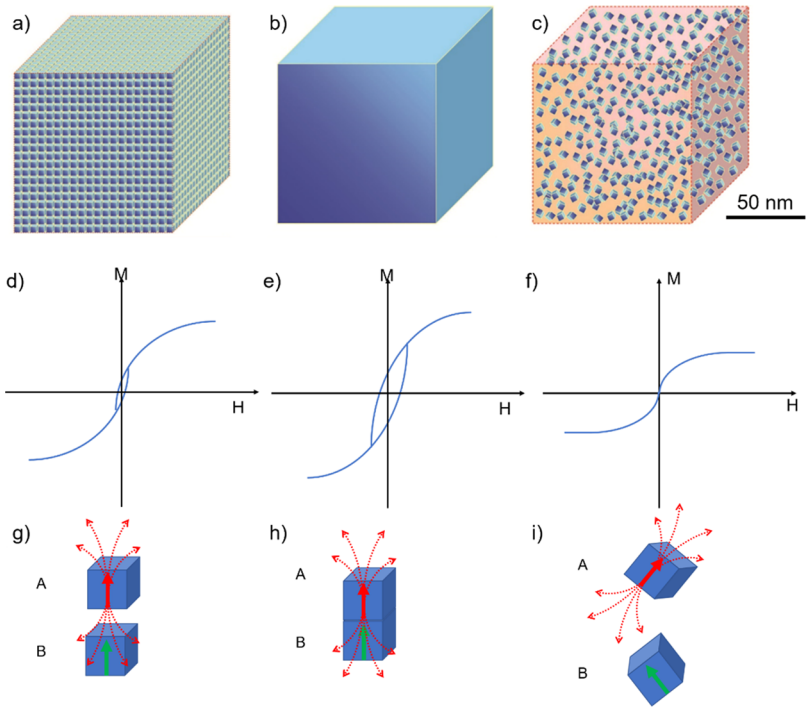

Figure 3. Schematic view of an NPC (a), a single-crystalline nanoparticle (b), and a nanocomposite (c). The corresponding schematic *M*−*H* curves and stray fields of small building blocks are also illustrated for these three particles of different structures. (d,g) NPC; (e,h) single-crystalline nanoparticle; and (f,i) nanocomposite.

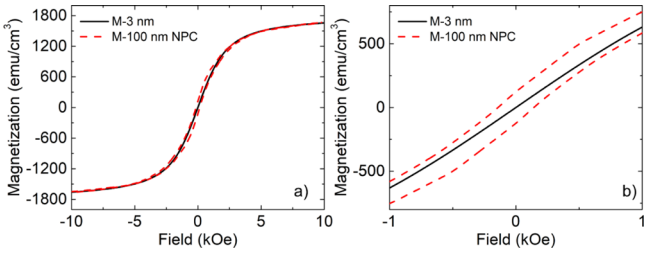

Figure 4. (a) Measured *M*−*H* curve of synthesized self-assembled 100 nm large, cubic FeCo NPCs in comparison with 3 nm cubic FeCo nanoparticles at room temperature, under a field range of −10 kOe to +10 kOe. (b) Zoomed-in view of (a) within a field range of −1 kOe to +1 kOe. "*M*" represents magnetization measured by the SQUID.

behavior with a non-zero coercivity, which is consistent with the theory of ferromagnetic materials. When an FeCo NPC is formed by self-assembly of these 3 nm nanoparticle units, the magnetic interactions between these small units can induce a magnetic vortex in the system, which result in the superparamagnetic behavior of FeCo NPC. Due to the long simulation time, we chose a simulation of 40 nm FeCo NPC to demonstrate our hypothesis. The simulation results of the FeCo NPC are shown in Figure 5b. In the hysteresis loop, the coercivity and remanence become zero, and the NPCs show superparamagnetic behavior. Several snapshots of magnetization patterns of the FeCo NPC are captured, and magnetic vortex is observed, which contributes to the transformation from ferromagnetic to superparamagnetic behavior. The reduced exchange interactions of these 3 nm nanoparticle units lead to the magnetic vortex structure and the superparamagnetic behavior. This result explains why the synthesized large FeCo NPCs show superparamagnetic behavior.

3.5. GPC Growth Model. To understand the formation mechanism of the large FeCo NPCs, we proposed a possible growth model for the GPC technique. The main effects are from the glow discharge and the drifting velocity of the carrying gas in the formation region of nanoparticles. A schematic diagram of the GPC system is shown in Figure 6, and there are two different areas that should be noted in the source chamber. The first is the region where nanoparticles are produced, and the other is the glow discharge region where large numbers of electrons and/or ions exist. These two regions can overlap, so the effect of glow discharge on the formation of nanoparticles should be carefully handled. Meanwhile, the Fe and Co atoms being knocked out of the target have a high energy of 10−50 eV.[57] Then, they are thermalized or cooled through collisions with argon atoms. The simulation and experimental results indicate that the maximum value of atom density occurs at the highest possible pressure in a high-pressure sputtering system (pressure is around 1 Torr),[58] Once the sputtered atoms are thermalized, they form supersaturated atom vapor if the atom density is high enough. At which point, nucleation occurs immediately followed by the growth process to form nanoparticles.[59,60]

The nucleation of nanoparticles happens near the sputtering target and then grow in the CDS region, as schematically illustrated in Figure 6. The further growth of these nanoparticles may happen in the NG region depending on the gas drifting velocity in the system. The further growth, also known as second crystallization, is like the first nucleation and growth processes in the CDS region, but the building blocks are small nanoparticles instead of the sputtered atoms from the target. There are two factors that define this second crystallization: the concentration and the temperature of the FeCo nanoparticles. If the temperature is too high and/or the concentration is too low, FeCo nanoparticles cannot nucleate/grow into FeCo NPCs. FeCo nanoparticles will, therefore, be limited to a size of around 3 nm under these

https://doi.org/10.1021/acsanm.1c01870
ACS Appl. Nano Mater. 2021, 4, 9382−9390

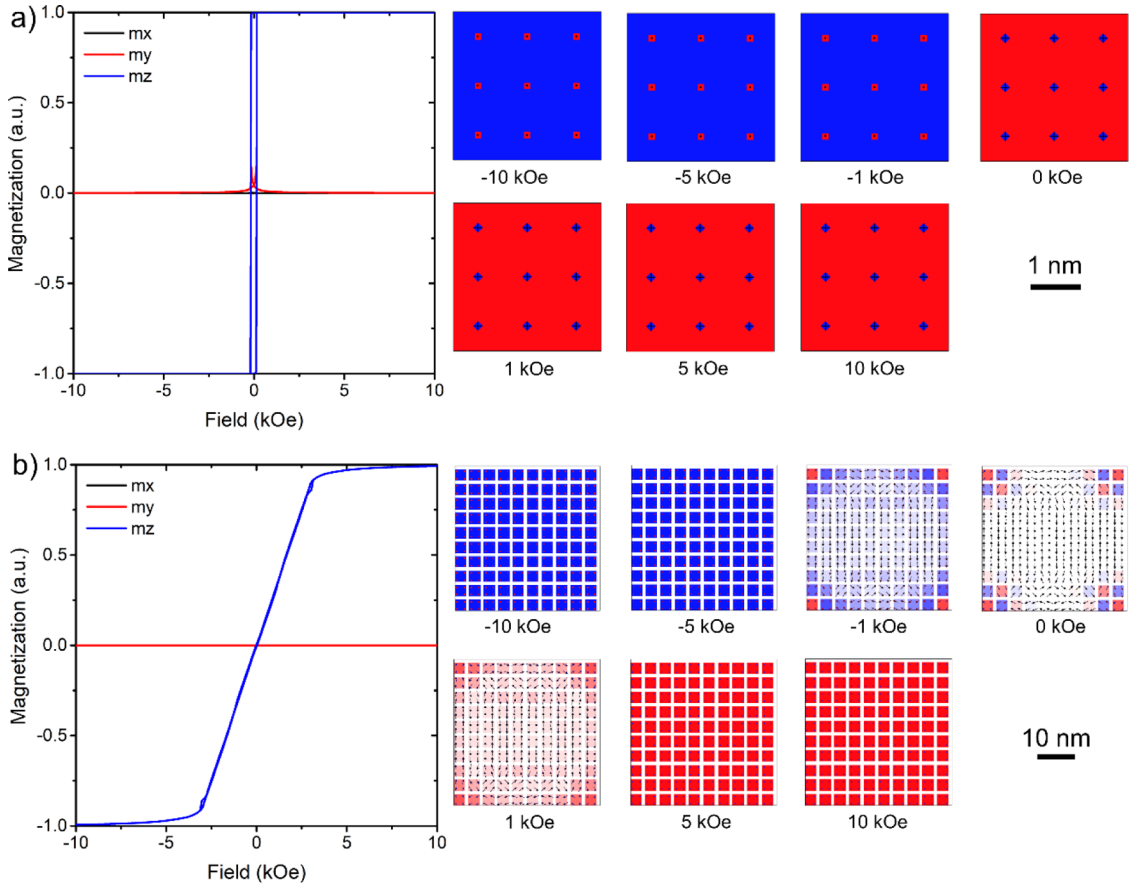

Figure 5. (a) $M-H$ curve and magnetization patterns of one 3 nm nanoparticle unit. The $M-H$ curve indicates that the unit is ferromagnetic with non-zero coercivity and remanence. (b) $M-H$ curve and magnetization patterns of one FeCo NPC composed of a 10 × 10 × 10 array of 3 nm FeCo nanoparticle units separated by 1 nm gaps. The $M-H$ curve of the FeCo NPC is superparamagnetic due to the reduced magnetic interactions between these 3 nm nanoparticle units. The panels on the right are the $x-y$ plane magnetization patterns of one 3 nm nanoparticle (top) and one 40 nm NPC (bottom), respectively, under a z-direction magnetic field of −10, −5, −1, 0, 1, 5, and 10 kOe.

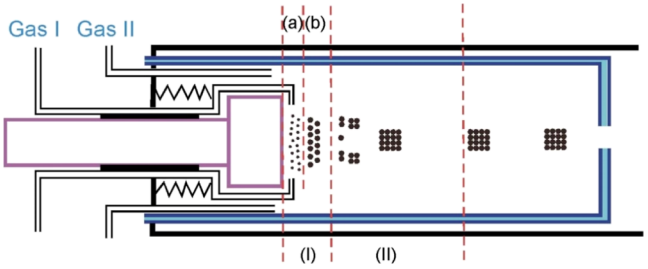

Figure 6. Schematic drawing of the nanoparticle source equipped with a magnetron DC sputtering gun. Region (I) is the CDS, where Ar^+ is dominant. Region (II) is the NG region, where both Ar^+ and electrons coexist. In region (a), sputtered atoms are predominantly neutral, where only one of a thousand atoms is positively charged. In region (b), small and charged nanoparticles are formed. In region (II), the small positively charged nanoparticles are neutralized and form nanoparticles or large nanoparticle assemblies through a secondary nucleation/growth process. Gases I and II are used to induce argon gas that functions as the sputtering and carrying gas.

conditions. If the temperature is low enough and/or the concentration is high enough, the FeCo nanoparticles will collide with each other to minimize the energy, forming FeCo NPCs. The combination of the temperature and concentration of these small nanoparticles provides flexibility to produce any intermediate state of nanoparticles with different sizes and shapes. Both the temperature and concentration of the FeCo nanoparticles can be controlled by adjusting the sputtering current density and the carrying gas velocity. When the sputtering pressure is high (like 450 mTorr used in our experiment) and the carrying gas velocity is low, there is a lower temperature because of the cooling effect from the carrying gas on the nanoparticles and vice versa.

In our experiments, the gas pressure and the sputtering current density were fixed, but the drift velocity varied. Varying the drift velocity of the nanoparticles, which is proportional to the drift velocity of the carrying gas, alters the temperature of the positively charged FeCo nanoparticles in the NG region. Since the temperature of the FeCo nanoparticles arriving at the NG region is determined by the number of collisions between the formed FeCo nanoparticles and argon atoms in the CDS, a faster drift velocity results in a higher temperature of FeCo nanoparticles (see Section S2 of Supporting Information for more details).

3.6. From FeCo Nanoparticles to NPCs: Fine Tuning Gas Flow Configuration. The gas flow configuration in the GPC system was simulated using FemLab (an interactive environment for modeling and simulating scientific problems based on partial differential equations) from COMSOL, as shown in Figure 7a,b. In the simulation, the gas was either injected from the inside position (Figure 7a) or from the outside position (Figure 7b). The profile of the gas pressure and velocity are depicted in Figure 7c,d, where the solid line is

https://doi.org/10.1021/acsanm.1c01870
ACS Appl. Nano Mater. 2021, 4, 9382−9390

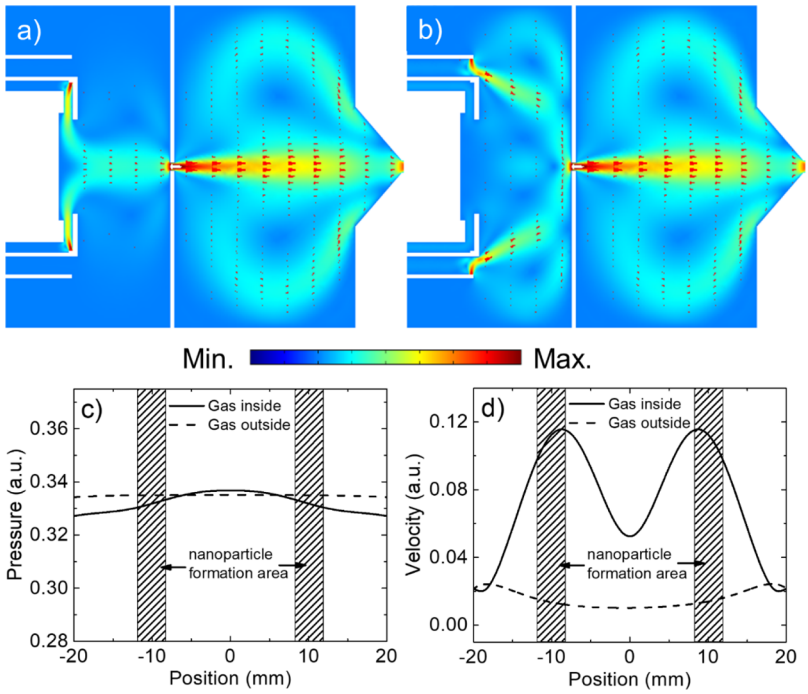

Figure 7. Simulated configuration of the gas velocity and gas pressure in the nanoparticle source with the different gas inlet positions: the inside gas inlet (a) and the outside gas inlet (b). The color denotes the gas pressure, and the arrow denotes the velocity. The profile of the gas pressure and velocity crossing a plane close to the cathode (c,d) are depicted. The pressure (c) and velocity (d) measurements are shown in the direction from the cathode to anode.

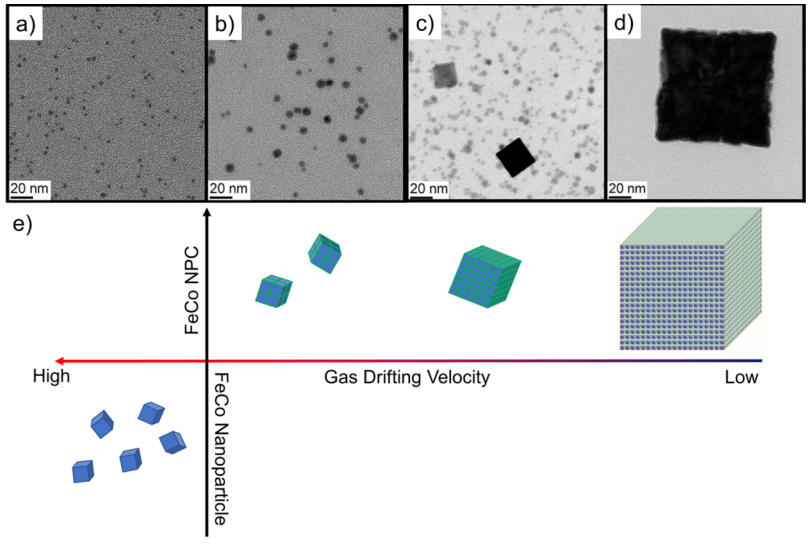

Figure 8. TEM images of FeCo nanoparticles and NPCs fabricated at different carrying gas velocities (the direction is from the cathode pointing to the anode). The carrying gas velocity was steadily decreased from (a) to (d). A schematic drawing of the relationship between the growth model of FeCo nanoparticles and FeCo NPCs and the gas drifting velocity (e).

for the gas injected inside and the dashed line is for the gas injected outside. Two nanoparticle formation areas are indicated in the figure, which relate to the formation of nanoparticles in the CDS and NG regions. The cathode position is at −20 mm. It is clear that at the same gas flow rate, (i) the velocity of the gas in the region close to the cathode changes dramatically with the different gas inlet positions, while the gas pressure shows no obvious difference; (ii) the gas velocity and pressure crossing the cathode surface is much more uniform when the gas is injected from the outside inlet position rather than the inside inlet position; and (iii) the velocity of the gas in the nanoparticle growth region can be controlled by changing the gas flow rate when alternating the inside and outside gas inlet positions.

According to the second crystallization mechanism of nanoparticles described above, when the experimental parameters are at the fixed gas pressure and sputtering current density, it can be expected that a high gas drifting velocity will result in a small nanoparticle size. A low gas velocity, however, will cause FeCo nanoparticles to self-assemble into large FeCo NPCs. Figure 8 shows the bright field TEM images of FeCo nanoparticles or NPCs prepared at different gas drifting

https://doi.org/10.1021/acsanm.1c01870
ACS Appl. Nano Mater. 2021, 4, 9382−9390

velocities. With the highest gas drifting velocity, only FeCo nanoparticles of ~3 nm were synthesized, as shown in Figure 8a. As the gas drifting velocity decreased, nanoparticle size started to increase, as shown in Figure 8b where the average FeCo nanoparticle size was ~7 nm. Further decreasing the gas drifting velocity resulted in the appearance of large cubic FeCo NPCs of 30 nm (Figure 8c); while at the lowest gas velocity (Figure 8d), only FeCo NPCs of ~100 nm were found. Figure 8e summarizes a schematic growth model of FeCo nanoparticles or NPCs related to the gas drifting velocity. At the high end of the gas drifting velocity, small FeCo nanoparticles are obtained, while the formation of FeCo NPCs starts with a decrease in the gas drifting velocity.

4. CONCLUSIONS AND PERSPECTIVES

In conclusion, 100 nm, cubic, FeCo NPCs with superparamagnetic behaviors were successfully synthesized using a sputtering-based GPC method. The nanoparticle formation mechanism of the second crystallization process was investigated. A glow discharge was used to produce supersaturated atom vapor in high pressure argon gas, and FeCo nanoparticles of 3 nm were formed through the primary nucleation and growth processes. By controlling the relative position of glow discharges and particle formation region, the FeCo nanoparticles were synthesized to be either nanoparticles or self-assembled NPCs through a secondary nucleation and growth process. TEM observation showed that these self-assembled FeCo NPCs consisted of small bcc-structured FeCo nanoparticle units of 3 nm with a 3D alignment of the crystal axis. The results also indicated that FeCo NPCs have a huge surface-area-to-volume ratio and similar superparamagnetic behavior as that of individual building blocks at room temperature. This work reported herein has provided a solution for synthesizing larger sized nanoparticles with superparamagnetic properties, overcoming the limitation on the size for SPMNPs in magnetic theranostics applications.

Recently, new GPC techniques for synthesizing nanoparticles are developed, such as GPC systems with multi-sources and a hollow source, which might be potentially used for synthesizing FeCo NPCs. A multi-sources GPC system is good for preparing NPCs/NPs with a core@shell structure.[61] A hollow-source GPC system is designed to enhance the target utilization rate and the yield of NPs.[62] These FeCo NPCs can potentially bring a higher sensitivity to the existing magnetic bioassay platforms. They are especially useful for detecting a very low amount of target analytes, where these NPCs with high magnetic moments may still be detectable by external magnetic sensors. Due to high magnetic moments of FeCo NPCs, a much lower dose is required for drug delivery and hyperthermia. Thus, it may avoid the risks of iron overdose. Similarly, compared with the iron oxide MNPs, a lower weight of FeCo NPCs is needed for magnetic imaging and magnetic separation, without degrading the performance. Extensive studies have also been reported to reduce the cytotoxicity of FeCo nanoparticles for biomedical applications, such as using oleic acid and carbon coatings.[27,63,64]

■ ASSOCIATED CONTENT

Supporting Information

The Supporting Information is available free of charge at https://pubs.acs.org/doi/10.1021/acsanm.1c01870.

Superparamagnetic properties of FeCo nanoparticles and growth model of nanoparticles and NPCs (PDF)

■ AUTHOR INFORMATION

Corresponding Author

Jian-Ping Wang − *Department of Electrical and Computer Engineering, University of Minnesota, Minneapolis, Minnesota 55455, United States*; Email: jpwang@umn.edu

Authors

Jinming Liu − *Department of Electrical and Computer Engineering, University of Minnesota, Minneapolis, Minnesota 55455, United States*; orcid.org/0000-0002-4313-5816

Kai Wu − *Department of Electrical and Computer Engineering, University of Minnesota, Minneapolis, Minnesota 55455, United States*; orcid.org/0000-0002-9444-6112

Shihai He − *Department of Electrical and Computer Engineering, University of Minnesota, Minneapolis, Minnesota 55455, United States*

Jianmin Bai − *Department of Electrical and Computer Engineering, University of Minnesota, Minneapolis, Minnesota 55455, United States*

Yun-Hao Xu − *Department of Electrical and Computer Engineering, University of Minnesota, Minneapolis, Minnesota 55455, United States*

Complete contact information is available at: https://pubs.acs.org/10.1021/acsanm.1c01870

Author Contributions

†J.L. and K.W. contributed equally to this work.

Notes

The authors declare no competing financial interest.

■ ACKNOWLEDGMENTS

Parts of this work were carried out in the Characterization Facility, University of Minnesota, which receives partial support from the NSF through the MRSEC (award no DMR-2011401) and the NNCI (award no ECCS-2025124) programs. Portions of this work were conducted in the Minnesota Nano Center, which is supported by the National Science Foundation through the National Nano Coordinated Infrastructure Network (NNCI) under Award no ECCS-1542202. The authors thank the Institute of Rock Magnetism, University of Minnesota, for the use of instruments for magnetism measurements.

■ REFERENCES

(1) Wu, K.; Su, D.; Liu, J.; Saha, R.; Wang, J.-P. Magnetic Nanoparticles in Nanomedicine: A Review of Recent Advances. *Nanotechnology* **2019**, *30*, 502003.

(2) Choi, J.; Gani, A. W.; Bechstein, D. J. B.; Lee, J.-R.; Utz, P. J.; Wang, S. X. Portable, One-Step, and Rapid GMR Biosensor Platform with Smartphone Interface. *Biosens. Bioelectron.* **2016**, *85*, 1−7.

(3) Gao, Y.; Huo, W.; Zhang, L.; Lian, J.; Tao, W.; Song, C.; Tang, J.; Shi, S.; Gao, Y. Multiplex Measurement of Twelve Tumor Markers Using a GMR Multi-Biomarker Immunoassay Biosensor. *Biosens. Bioelectron.* **2019**, *123*, 204−210.

(4) Lee, H.; Sun, E.; Ham, D.; Weissleder, R. Chip−NMR Biosensor for Detection and Molecular Analysis of Cells. *Nat. Med.* **2008**, *14*, 869.

(5) Wu, K.; Liu, J.; Saha, R.; Su, D.; Krishna, V. D.; Cheeran, M. C.-J.; Wang, J.-P. Magnetic Particle Spectroscopy for Detection of

Influenza A Virus Subtype H1N1. *ACS Appl. Mater. Interfaces* **2020**, *12*, 13686−13697.
(6) Wu, K.; Klein, T.; Krishna, V. D.; Su, D.; Perez, A. M.; Wang, J.-P. Portable GMR Handheld Platform for the Detection of Influenza A Virus. *ACS Sens.* **2017**, *2*, 1594−1601.
(7) Johannsen, M.; Thiesen, B.; Wust, P.; Jordan, A. Magnetic Nanoparticle Hyperthermia for Prostate Cancer. *Int. J. Hyperther.* **2010**, *26*, 790−795.
(8) Jing, Y.; He, S.-H.; Wang, J.-P. Fe3Si Nanoparticles for Alternating Magnetic Field Heating. *J. Nanoparticle Res.* **2013**, *15*, 1517.
(9) Bañobre-López, M.; Teijeiro, A.; Rivas, J. Magnetic Nanoparticle-Based Hyperthermia for Cancer Treatment. *Rep. Pract. Oncol. Radiother.* **2013**, *18*, 397−400.
(10) Wu, K.; Wang, J.-P. Magnetic Hyperthermia Performance of Magnetite Nanoparticle Assemblies under Different Driving Fields. *AIP Adv.* **2017**, *7*, 056327.
(11) Yu, L.; Liu, J.; Wu, K.; Klein, T.; Jiang, Y.; Wang, J.-P. Evaluation of Hyperthermia of Magnetic Nanoparticles by Dehydrating DNA. *Sci. Rep.* **2014**, *4*, 7216.
(12) Lee, N.; Hyeon, T. Designed Synthesis of Uniformly Sized Iron Oxide Nanoparticles for Efficient Magnetic Resonance Imaging Contrast Agents. *Chem. Soc. Rev.* **2012**, *41*, 2575−2589.
(13) Golestanirad, L.; Kirsch, J.; Bonmassar, G.; Downs, S.; Elahi, B.; Martin, A.; Iacono, M.-I.; Angelone, L. M.; Keil, B.; Wald, L. L.; Pilitsis, J. RF-Induced Heating in Tissue near Bilateral DBS Implants during MRI at 1.5 T and 3T: The Role of Surgical Lead Management. *Neuroimage* **2019**, *184*, 566−576.
(14) Vargas-Osorio, Z.; Argibay, B.; Piñeiro, Y.; Vázquez-Vázquez, C.; López-Quintela, M. A.; Alvarez-Perez, M. A.; Sobrino, T.; Campos, F.; Castillo, J.; Rivas, J. Multicore Magnetic Fe 3 O 4@ C Beads with Enhanced Magnetic Response for MRI in Brain Biomedical Applications. *IEEE Trans. Magn.* **2016**, *52*, 1−4.
(15) Barrow, M.; Taylor, A.; Murray, P.; Rosseinsky, M. J.; Adams, D. J. Design Considerations for the Synthesis of Polymer Coated Iron Oxide Nanoparticles for Stem Cell Labelling and Tracking Using MRI. *Chem. Soc. Rev.* **2015**, *44*, 6733−6748.
(16) Bao, G.; Mitragotri, S.; Tong, S. Multifunctional Nanoparticles for Drug Delivery and Molecular Imaging. *Annu. Rev. Biomed. Eng.* **2013**, *15*, 253−282.
(17) Chowdhuri, A. R.; Bhattacharya, D.; Sahu, S. K. Magnetic Nanoscale Metal Organic Frameworks for Potential Targeted Anticancer Drug Delivery, Imaging and as an MRI Contrast Agent. *Dalton Trans.* **2016**, *45*, 2963−2973.
(18) Zhao, Y.; Luo, Z.; Li, M.; Qu, Q.; Ma, X.; Yu, S.-H.; Zhao, Y. A Preloaded Amorphous Calcium Carbonate/Doxorubicin@ Silica Nanoreactor for PH-Responsive Delivery of an Anticancer Drug. *Angew. Chem., Int. Ed.* **2015**, *54*, 919−922.
(19) Yew, Y. P.; Shameli, K.; Miyake, M.; Khairudin, N. B. B. A.; Mohamad, S. E. B.; Naiki, T.; Lee, K. X. Green Biosynthesis of Superparamagnetic Magnetite Fe3O4 Nanoparticles and Biomedical Applications in Targeted Anticancer Drug Delivery System: A Review. *Arabian J. Chem.* **2020**, *13*, 2287−2308.
(20) Vallabani, N. V. S.; Singh, S. Recent Advances and Future Prospects of Iron Oxide Nanoparticles in Biomedicine and Diagnostics. *3 Biotech* **2018**, *8*, 279.
(21) Wu, K.; Liu, J.; Saha, R.; Ma, B.; Su, D.; Peng, C.; Sun, J.; Wang, J.-P. Irregularly Shaped Iron Nitride Nanoparticles as a Potential Candidate for Biomedical Applications: From Synthesis to Characterization. *ACS Omega* **2020**, *5*, 11756−11767.
(22) Colombo, M.; Carregal-Romero, S.; Casula, M. F.; Gutiérrez, L.; Morales, M. P.; Böhm, I. B.; Heverhagen, J. T.; Prosperi, D.; Parak, W. J. Biological Applications of Magnetic Nanoparticles. *Chem. Soc. Rev.* **2012**, *41*, 4306−4334.
(23) Srinivasan, B.; Li, Y.; Jing, Y.; Xu, Y.; Yao, X.; Xing, C.; Wang, J.-P. A Detection System Based on Giant Magnetoresistive Sensors and High-moment Magnetic Nanoparticles Demonstrates Zeptomole Sensitivity: Potential for Personalized Medicine. *Angew. Chem., Int. Ed.* **2009**, *48*, 2764−2767.
(24) Burkert, T.; Nordström, L.; Eriksson, O.; Heinonen, O. Giant Magnetic Anisotropy in Tetragonal FeCo Alloys. *Phys. Rev. Lett.* **2004**, *93*, 027203.
(25) Andersson, G.; Burkert, T.; Warnicke, P.; Björck, M.; Sanyal, B.; Chacon, C.; Zlotea, C.; Nordström, L.; Nordblad, P.; Eriksson, O. Perpendicular Magnetocrystalline Anisotropy in Tetragonally Distorted Fe-Co Alloys. *Phys. Rev. Lett.* **2006**, *96*, 037205.
(26) Gao, T. R.; Wu, Y. Q.; Fackler, S.; Kierzewski, I.; Zhang, Y.; Mehta, a.; Kramer, M. J.; Takeuchi, I. Combinatorial Exploration of Rare-Earth-Free Permanent Magnets: Magnetic and Microstructural Properties of Fe-Co-W Thin Films. *Appl. Phys. Lett.* **2013**, *102*, 022419.
(27) Song, G.; Kenney, M.; Chen, Y.-S.; Zheng, X.; Deng, Y.; Chen, Z.; Wang, S. X.; Gambhir, S. S.; Dai, H.; Rao, J. Carbon-Coated FeCo Nanoparticles as Sensitive Magnetic-Particle-Imaging Tracers with Photothermal and Magnetothermal Properties. *Nat. Biomed. Eng.* **2020**, *4*, 325−334.
(28) Liu, J.; Su, D.; Wu, K.; Wang, J.-P. High-Moment Magnetic Nanoparticles. *J. Nanoparticle Res.* **2020**, *22*, 66.
(29) Sanità, G.; Carrese, B.; Lamberti, A. Nanoparticle Surface Functionalization: How to Improve Biocompatibility and Cellular Internalization. *Front. Mol. Biosci.* **2020**, *7*, 587012.
(30) Kotha, R.; Fernandes, G.; Nikam, A. N.; Kulkarni, S.; Pandey, A.; Pandey, S.; Mutalik, S. Surface Engineered Bimetallic Nanoparticles Based Therapeutic and Imaging Platform: Recent Advancements and Future Perspective. *Mater. Sci. Technol.* **2020**, *36*, 1729−1748.
(31) Jing, Y.; Sohn, H.; Kline, T.; Victora, R. H.; Wang, J.-P. Experimental and Theoretical Investigation of Cubic FeCo Nanoparticles for Magnetic Hyperthermia. *J. Appl. Phys.* **2009**, *105*, 07B305.
(32) Kolhatkar, A.; Jamison, A.; Litvinov, D.; Willson, R.; Lee, T. Tuning the Magnetic Properties of Nanoparticles. *Int. J. Mol. Sci.* **2013**, *14*, 15977−16009.
(33) Singamaneni, S.; Bliznyuk, V. N.; Binek, C.; Tsymbal, E. Y. Magnetic Nanoparticles: Recent Advances in Synthesis, Self-Assembly and Applications. *J. Mater. Chem.* **2011**, *21*, 16819−16845.
(34) Krishnan, K. M. Biomedical Nanomagnetics: A Spin through Possibilities in Imaging, Diagnostics, and Therapy. *IEEE Trans. Magn.* **2010**, *46*, 2523−2558.
(35) Zhou, X.; Yin, Y.-X.; Wan, L.-J.; Guo, Y.-G. Self-Assembled Nanocomposite of Silicon Nanoparticles Encapsulated in Graphene through Electrostatic Attraction for Lithium-Ion Batteries. *Adv. Energy Mater.* **2012**, *2*, 1086−1090.
(36) Lee, S. H.; Yu, S.-H.; Lee, J. E.; Jin, A.; Lee, D. J.; Lee, N.; Jo, H.; Shin, K.; Ahn, T.-Y.; Kim, Y.-W.; Choe, H.; Sung, Y.-E.; Hyeon, T. Self-Assembled Fe3O4 Nanoparticle Clusters as High-Performance Anodes for Lithium Ion Batteries via Geometric Confinement. *Nano Lett.* **2013**, *13*, 4249−4256.
(37) Ge, J.; Hu, Y.; Yin, Y. Highly Tunable Superparamagnetic Colloidal Photonic Crystals. *Angew. Chem., Int. Ed. Engl.* **2007**, *46*, 7428−7431.
(38) Li, Y.; Koshizaki, N.; Cai, W. Periodic One-Dimensional Nanostructured Arrays Based on Colloidal Templates, Applications, and Devices. *Coord. Chem. Rev.* **2011**, *255*, 357−373.
(39) Zhang, J.; Li, Y.; Zhang, X.; Yang, B. Colloidal Self-Assembly Meets Nanofabrication: From Two-Dimensional Colloidal Crystals to Nanostructure Arrays. *Adv. Mater.* **2010**, *22*, 4249−4269.
(40) Ravnik, M.; Alexander, G. P.; Yeomans, J. M.; Žumer, S. Three-Dimensional Colloidal Crystals in Liquid Crystalline Blue Phases. *Proc. Natl. Acad. Sci. U.S.A.* **2011**, *108*, 5188−5192.
(41) Hugounenq, P.; Levy, M.; Alloyeau, D.; Lartigue, L.; Dubois, E.; Cabuil, V.; Ricolleau, C.; Roux, S.; Wilhelm, C.; Gazeau, F.; Bazzi, R. Iron Oxide Monocrystalline Nanoflowers for Highly Efficient Magnetic Hyperthermia. *J. Phys. Chem. C* **2012**, *116*, 15702−15712.
(42) Vystavel, T.; Koch, S. A.; Palasantzas, G.; De Hosson, J. T. M. Structural Dynamics of Gas-Phase Molybdenum Nanoclusters: A Transmission Electron Microscopy Study. *Appl. Phys. Lett.* **2005**, *86*, 113113.

https://doi.org/10.1021/acsanm.1c01870
ACS Appl. Nano Mater. 2021, 4, 9382−9390

(43) Krishnan, G.; Verheijen, M. A.; ten Brink, G. H.; Palasantzas, G.; Kooi, B. J. Tuning Structural Motifs and Alloying of Bulk Immiscible Mo-Cu Bimetallic Nanoparticles by Gas-Phase Synthesis. *Nanoscale* **2013**, *5*, 5375−5383.
(44) Lartigue, L.; Hugounenq, P.; Alloyeau, D.; Clarke, S. P.; Lévy, M.; Bacri, J.-C.; Bazzi, R.; Brougham, D. F.; Wilhelm, C.; Gazeau, F. Cooperative Organization in Iron Oxide Multi-Core Nanoparticles Potentiates Their Efficiency as Heating Mediators and MRI Contrast Agents. *ACS Nano* **2012**, *6*, 10935−10949.
(45) Qiu, J.-M.; Wang, J.-P. Tuning the Crystal Structure and Magnetic Properties of FePt Nanomagnets. *Adv. Mater.* **2007**, *19*, 1703−1706.
(46) He, S.; Jing, Y.; Wang, J.-P. Direct Synthesis of Large Size Ferromagnetic SmCo5 Nanoparticles by a Gas-Phase Condensation Method. *J. Appl. Phys.* **2013**, *113*, 134310.
(47) Xu, Y.-H.; Wang, J.-P. Direct Gas-Phase Synthesis of Heterostructured Nanoparticles through Phase Separation and Surface Segregation. *Adv. Mater.* **2008**, *20*, 994−999.
(48) Shield, J. E. Cluster-Assembled Magnetic Nanostructures and Materials. *Frontiers of Nanoscience*; Elsevier, 2020; Vol. *15*, pp 163−184.
(49) Ahmadi, Z.; Lu, H.; Mukherjee, P.; Koten, M.; Gruverman, A.; Shield, J. E. Resistive Switching in Individual Co/ZnO Core/Shell Nanoparticles Formed via Inert Gas Condensation and Selective Oxidation. *Adv. Electron. Mater.* **2020**, *6*, 2000065.
(50) Koten, M. A.; Voeller, S. A.; Patterson, M. M.; Shield, J. E. In Situ Measurements of Plasma Properties during Gas-Condensation of Cu Nanoparticles. *J. Appl. Phys.* **2016**, *119*, 114306.
(51) Balamurugan, B.; Skomski, R.; Li, X. Z.; Hadjipanayis, G. C.; Sellmyer, D. J. Magnetism of Directly Ordered Sm-Co Clusters. *J. Appl. Phys.* **2012**, *111*, 07B527.
(52) Balasubramanian, B.; Skomski, R.; Li, X.; Valloppilly, S. R.; Shield, J. E.; Hadjipanayis, G. C.; Sellmyer, D. J. Cluster Synthesis and Direct Ordering of Rare-Earth Transition-Metal Nanomagnets. *Nano Lett.* **2011**, *11*, 1747−1752.
(53) Lewis, M.; Bichoupan, K.; Shah, S. I.; Zide, J. M. O. Growth of ErAs Nanoparticles by Pulsed Laser Ablation in an Inert Environment. *J. Electron. Mater.* **2016**, *45*, 6247−6250.
(54) Jaffari, G. H.; Ceylan, A.; Bui, H. P.; Beebe, T. P., Jr.; Ozcan, S.; Shah, S. I. Non-Equilibrium Cation Distribution and Enhanced Spin Disorder in Hollow CoFe2O4 Nanoparticles. *J. Phys. Condens. Matter* **2012**, *24*, 336004.
(55) Liu, X.; Wang, J.-P. Fabrication and Morphologies of Large Directly Ordered L1[Sub 0] FePt Nanoparticles in Gas Phase. *J. Appl. Phys.* **2009**, *105*, 07A722.
(56) Liu, J.; Schliep, K.; He, S.-H.; Ma, B.; Jing, Y.; Flannigan, D. J.; Wang, J.-P. Iron Nanoparticles with Tunable Tetragonal Structure and Magnetic Properties. *Phys. Rev. Mater.* **2018**, *2*, 054415.
(57) Binns, C.; Maher, M. J.; Pankhurst, Q. A.; Kechrakos, D.; Trohidou, K. N. Magnetic Behavior of Nanostructured Films Assembled from Preformed Fe Clusters Embedded in Ag. *Phys. Rev. B: Condens. Matter Mater. Phys.* **2002**, *66*, 184413.
(58) Shon, C. H.; Lee, J. K. Modeling of Magnetron Sputtering Plasmas. *Appl. Surf. Sci.* **2002**, *192*, 258−269.
(59) Bogaerts, A. Comprehensive Modelling Network for Dc Glow Discharges in Argon. *Plasma Sources Sci. Technol.* **1999**, *8*, 210−229.
(60) Krasnochtchekov, P.; Albe, K.; Ashkenazy, Y.; Averback, R. S. Molecular-Dynamics Study of the Density Scaling of Inert Gas Condensation. *J. Chem. Phys.* **2005**, *123*, 154314.
(61) Huttel, Y.; Martínez, L.; Mayoral, A.; Fernández, I. Gas-Phase Synthesis of Nanoparticles: Present Status and Perspectives. *MRS Commun.* **2018**, *8*, 947.
(62) Liu, J.; He, S.-H.; Wang, J.-P. High-Yield Gas-Phase Condensation Synthesis of Nanoparticles to Enable a Wide Array of Applications. *ACS Appl. Nano Mater.* **2020**, *3*, 7942−7949.
(63) Hong, X.; Li, M.; Bao, N.; Peng, E.; Li, W.; Xue, J.; Ding, J. Synthesis of FeCo Nanoparticles from FeO (OH) and Co 3 O 4 Using Oleic Acid as Reduction Agent. *J. Nanoparticle Res.* **2014**, *16*, 1935.
(64) Park, J. K.; Jung, J.; Subramaniam, P.; Shah, B. P.; Kim, C.; Lee, J. K.; Cho, J.-H.; Lee, C.; Lee, K.-B. Graphite-Coated Magnetic Nanoparticles as Multimodal Imaging Probes and Cooperative Therapeutic Agents for Tumor Cells. *Small* **2011**, *7*, 1647−1652.

https://doi.org/10.1021/acsanm.1c01870
ACS Appl. Nano Mater. 2021, 4, 9382−9390